Graphene-based Plasmonic Switch using Resonant Coupling to the Local Plasmon Resonance

Kyungsun Moon[*] and SukYoung Park

Department of Physics and IPAP, Yonsei University, Seoul 03722, Korea

We theoretically study a graphene-based plasmonic waveguide composed of graphene, hexagonal boron nitride and active layer heterostructure, which can gate the transmission of a surface plasmon polariton (SPP) localized near the interface between the active layer and graphene. When a gate voltage is applied above a certain critical value, the charge-density modulation in the quasi-2D electron gas formed in the inversion layer can induce a local plasmon resonance. Since the local plasmon resonance is strongly coupled to the SPP, it can suppress the transmission of the SPP. The main advantage of our device lies in the sharpness of the switching line shape, since the operation manifests the underlying resonance phenomenon. By taking the active layer to be the p-type Si(100) layer, we calculate the propagation length of the SPP with varying gate voltage. We show that the wavelength of the SPP is reduced to approximately 1/100 of that of an incident light and the propagation length of the SPP is significantly reduced by a factor of approximately 20 upon switching. This ensures that our plasmonic waveguide can operate effectively as a plasmonic switch for the SPP.

I. INTRODUCTION

Recent technological advances in dynamically controlling the plasmon properties of photoactive materials have played an important role from data processing and transmission to energy harvesting [1–6]. Surface plasmon polaritons are electromagnetic excitations propagating at the interface between a dielectric and a metal, evanescently confined in the perpendicular direction. These electromagnetic surface waves arise due to the coupling of the electromagnetic fields in the dielectric to the charge-density fluctuations on the metal surface. Since their wavelengths are typically much shorter than that of an incident light, they have been successfully applied to the subwavelength optics in microscopy and lithography beyond the diffraction limit [7–11]. Photonic devices have great advantages over electronic ones due to the fast operation speed. However, large device size has remained as an obstacle for practical purpose. Hence the SPP can provide a breakthrough for miniaturization of photonic devices. Extensive studies have been performed to investigate the SPP dispersion relations for various waveguide structures both theoretically and experimentally [12–15]. For practical photonic device applications, high-Q-factor of the SPP is required and hence much efforts have been taken to increase the Q factor such as optimizing waveguide geometry and adopting low-loss materials [16]. In order to

control the SPP in a subwavelength photonic device, various methods have been proposed such as optical controls using heat, gate voltage, and light [1–6]. Since the coupling strength between the SPP and external fields such as gate voltage is relatively weak, they usually require high switching voltage and long channel length. Moreover, slow switching time typically shown in previous experiments is a great challenge to overcome in order to achieve high-speed information processing.

Graphene, a 2D sheet of carbon atoms placed on the honeycomb lattice, has attracted a lot of theoretical and experimental attention due to its superior physical properties such as high mobility, elastic, thermal, and optical properties [17–21]. The optical absorption rate of graphene has exhibited a universal value of $\pi\alpha \cong 2.3\%$ in the visible and near-infrared region, where α denotes the fine structure constant. This broadband absorption characteristic has been utilized for the graphene-based photodetectors and modulators [22,23]. In addition, the graphene plasmonic effects have been investigated for different applications ranging from light modulation to biological and chemical sensing [24–31]. It has been shown that the dispersion relation of a plasmonic slab waveguide is tuned by graphene contact and the spatially modulated doping in graphene tubes can modify the plasmonic band structure [32,33]. The 2D nature and high mobility of graphene have enabled an enhanced light-matter interaction and fast photodetection [34–36]. In this paper, we study the plasmonic waveguide, which controls the transmission of an incident
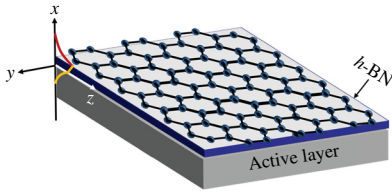
———————
[*]kmoon@yonsei.ac.kr

FIG. 1. Schematic of our plasmonic waveguide. Hexagonal boron nitride film is used as a gate dielectric material for graphene. The active layer is taken to be a p-type semiconductor with high mobility for sharp switching line shape such as p-type silicon. The SPP propagates along the z axis.

light by switching the coupling of the SPP localized at the graphene-semiconductor interface. The schematic of our device is illustrated in Fig. 1. Hexagonal boron nitride (*h*-BN) film is used as a gate dielectric material for graphene. Graphene-based electronic devices are actively developed in order to utilize the excellent electrical conduction characteristics of graphene. However, most of the experimental results do not show a dramatic increase in device efficiency as compared to theoretical prediction. As a van der Waals material, *h*-BN has performed well as a perfect substrate material for graphene, which can support the high mobility of graphene similar to the level of the suspended graphene flake [37]. The active layer is taken to be a p-type semiconductor with high mobility in order to achieve a fast switching. The energy band diagram of the plasmonic waveguide is shown in Fig. 2. The top gate is separated from the graphene layer by an air gap [38]. The air gate structure is devised to control electrically the Fermi energy of the graphene layer. Since we do not intend to confine the electromagnetic field of the surface plasmon polariton by the top metal gate, it is not required to fully cover the top surface of the graphene layer. Hence it only partially impedes the optical access to the graphene layer by the experimentally ingenious design of the air gate structure. By utilizing the double-gate geometry with
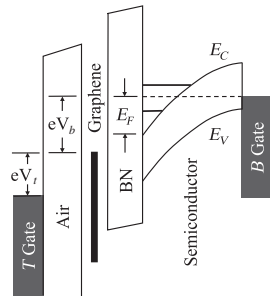
both the top and bottom gate, one can control the Fermi energy of graphene by varying the top-gate voltage V_t. The electrostatic potential energy in the p-type semiconductor is spatially modulated by varying the bottom-gate voltage V_b, which leads to band bending. The operating principle of our device is as follows. When the negative bottom-gate voltage is applied below a certain threshold value, an inversion layer appears within the depletion region of a p-type semiconductor and quasi-2D electron gas is formed in the inversion layer. By lowering the bottom-gate voltage further, one can increase the total number of electrons in the 2D electron gas and spatially modulate the electron number density as well. Above a certain critical voltage, it can induce a local plasmon resonance in the inversion layer. Due to the strong coupling of the SPP to the local plasmon resonance, the transmission of the SPP is strongly suppressed in our plasmonic waveguide.

In spite of high electron mobility, GaAs has the experimental implementation challenge of overcoming surface depletion due to Fermi-level pinning at the surface. Hence we choose the p-type Si(100) as an active layer. For the experimentally available set of parameters, we calculate that for an incident light with midinfrared wavelength $\lambda = 8~\mu$m, the wavelength of the SPP is reduced to approximately $1/100$ of that of an incident light. Upon approaching the threshold voltage, the propagation length of the SPP has been dramatically reduced by a factor of approximately 20 upon switching. Hence our plasmonic switch can effectively gate the transmission of the SPP by applying a gate voltage. Since the gating operation reflects upon the underlying resonance phenomenon, our plasmonic waveguide demonstrates much sharper switching line shape in comparison to the other devices [27]. Recently it has been experimentally demonstrated that a pumped laser pulse can modulate the carrier density by about 6% in the ITO and nanoantennae hybrid structure [6]. For the future application to all-optical plasmonic switch, our device has sharpness characteristic, which is operative to such a modest density modulation.

II. THEORY FOR GRAPHENE-BASED PLASMONIC SWITCH

We investigate the physical properties of the SPP in our plasmonic waveguide. The magnetic field in the transverse magnetic (TM) mode of our waveguide is described by $\tilde{H}(x,y,z) = \tilde{H}(x) \exp\left[i(k_z z - \omega t)\right] \hat{y}$, which propagates along the z axis with frequency ω and wave number k_z. It satisfies the following nonuniform wave equation [11,39]:

FIG. 2. Energy band diagram of the plasmonic waveguide. Graphene is separated from the top gate by an air gap. The top-gate voltage V_t can control the Fermi energy of graphene and the bottom-gate voltage V_b can modulate the electrostatic potential energy profile in the inversion layer.

$$\frac{\partial^2 \tilde{H}}{\partial x^2} - \frac{1}{\epsilon(\omega,x)} \frac{d\epsilon(x)}{dx} \frac{\partial \tilde{H}}{\partial x} - \left[k_z^2 - k^2 \epsilon(\omega,x)\right] \tilde{H} = 0,$$
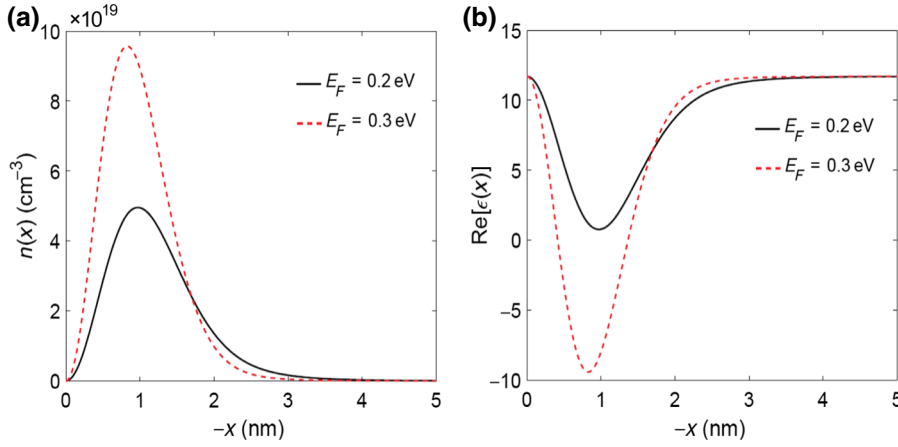
(1)

FIG. 3. (a) Electron number densities $n(x)$ are plotted as a function of $-x$ for $E_F = 0.2, 0.3$ eV. (b) The real parts of dielectric permittivities Re $[\epsilon(x)]$ are plotted as a function of $-x$ for $E_F = 0.2, 0.3$ eV.

where k represents the wave number of the incident light in free space and $\epsilon(\omega, x)$ the relative permittivity at frequency ω as a function of position x. The impedance of a waveguide is defined by $Z = E_z/H_y$ with $E_z = [i/k\epsilon(\omega, x)] \left(\partial H_y/\partial x\right) \sqrt{\mu_0/\epsilon_0}$. The dimensionless impedance $Z(x)$ in units of $\sqrt{\mu_0/\epsilon_0}$ obeys the following nonuniform wave equation, which is written as

$$\frac{\partial Z}{\partial x} + ik \left[1 - \epsilon(\omega, x)Z^2 - \frac{k_z^2}{k^2\epsilon(\omega, x)} \right] = 0. \quad (2)$$

In our plasmonic waveguide, we take the p-type semiconductor as an active layer, whose relative permittivity $\epsilon(\omega, x)$ is spatially modulated by applying the bottom-gate voltage. According to the Drude model, $\epsilon(\omega, x)$ in the active layer depends on the local plasma frequency $\omega_p(x)$ as follows:

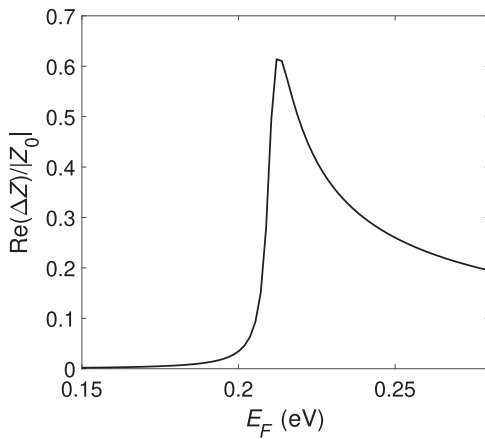$$\epsilon(\omega, x) = \epsilon_\infty - \frac{\omega_p^2(x)}{\omega(\omega + i\nu)}, \quad (3)$$

where $\omega_p(x)$ depends on the local electron number density $n(x)$ through $\omega_p(x) = \sqrt{n(x)e^2/m_c^*\epsilon_0}$ with m_c^* being the effective mass for conductivity and ϵ_∞, ν representing the high-frequency relative permittivity and the plasma damping rate of the active layer, respectively.

Now we explain how to obtain the spatial dependence of the electron number density $n(x)$ for a given Fermi energy E_F of the quasi-2D electron gas. In the semiconductor quantum-well heterostructures, the translation symmetry along the x axis is explicitly broken and hence the bulk symmetry-related ellipsoidal electron and hole pockets are split into distinct groups with different sets of effective masses depending on the crystal plane of the semiconductor. An electron confined in a quantum well described by the potential energy $V(x)$ satisfies the following Schrödinger equation:

$$-\frac{\hbar^2}{2m_{x\mu}} \frac{d^2\Psi_{i\mu}(x)}{dx^2} + \left[V(x) - E_{i\mu}\right] \Psi_{i\mu}(x) = 0, \quad (4)$$

FIG. 4. The real part of impedance change at the top of the p-type Si(100) substrate as a function of the Fermi energy E_F in units of $|Z_0|$ for $\lambda = 8$ μm. It demonstrates a dramatic increase of Re(ΔZ) above $E_F^* \cong 0.21$ eV.
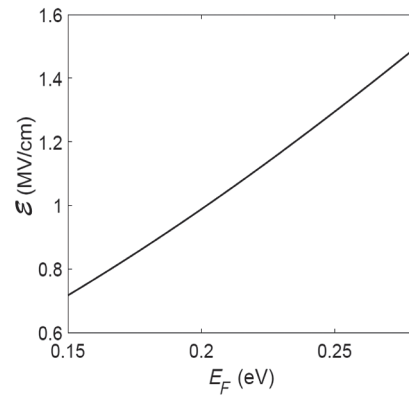

FIG. 5. Electric field strength $\mathcal{E}$ at the gate dielectric-semiconductor interface as a function of the Fermi energy E_F for $\lambda = 8$ μm. At the critical value of $E_F^* \cong 0.21$ eV, $\mathcal{E} \cong 1.0$ MV/cm.
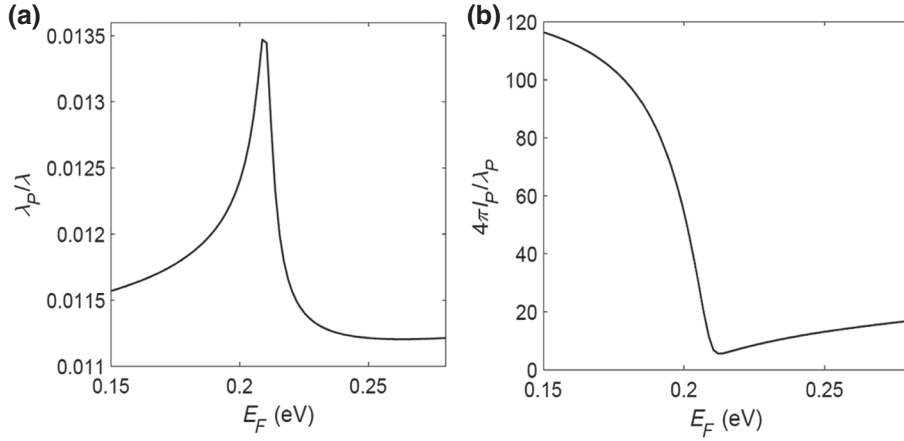
FIG. 6. (a) The wavelength of the SPP is plotted as a function of E_F in units of λ. The wavelength λ_p of the SPP shows a nonmonotonic dependence on E_F, as it passes through the critical value. But it remains to be on the order of approximately 1/100 of that of an incident light. (b) The ratio of the propagation length to the wavelength of the SPP is plotted as a function of E_F. One can notice that $4\pi l_p/\lambda_p$ is significantly reduced by a factor of approximately 21 upon switching at $E_F^* \cong 0.21$ eV compared to the value at $E_F = 0.15$ eV.

where $m_{x\mu}$ represents the effective mass along the x axis for the μth group with the distinct set of effective masses and the index i denotes the ith electric subband. The electrostatic potential $\Phi(x) = -V(x)/e$ satisfies the Gauss law:

$$\frac{d^2\Phi(x)}{dx^2} = \frac{e}{\epsilon_s}\left[n(x) - p(x) + N_a\right], \qquad (5)$$

where $\epsilon_s, n(x), p(x)$ represent the dielectric permittivity of the semiconductor, the electron number density, and the hole number density, respectively, and N_a the doping concentration of acceptor impurities. One can assume that $p(x)$ is negligibly small within the depletion region [40]. For the low-energy electric subband strongly localized to the gate dielectric-semiconductor interface, the electrostatic potential energy is well approximated by $V(x) = e\mathcal{E}x$ for $x > 0$ with an infinite potential barrier at $x = 0$. The electric field strength $\mathcal{E}$ is determined self-consistently. The energy eigenfunction of the ith subband in the μth group is written by Airy function with normalization constant $N_{i\mu}$ such that $\Psi_{i\mu}(x) = N_{i\mu}\text{Ai}(\tilde{x}_{i\mu})$, where the dimensionless coordinate $\tilde{x}_{i\mu} = x/a_\mu + s_i$ with s_i being the ith zero of the Airy function and $a_\mu = \left[\hbar^2/\left(2m_{x\mu}e\mathcal{E}\right)\right]^{1/3}$ [40]. The energy eigenvalues are given by $E_{i\mu} = -\left(e\mathcal{E}a_\mu\right)s_i$. At temperature T, the electron number density $n(x)$ is written as

$$n(x) = \left(\frac{k_BT}{\pi\hbar^2}\right)\sum_{i=1}^{\infty}\sum_{\mu}n_{v\mu}m_{d\mu}\ln\left[1 + e^{(E_F-E_{i\mu})/k_BT}\right]$$
$$\times N_{i\mu}^2\text{Ai}^2\left(x/a_\mu + s_i\right), \qquad (6)$$

where $m_{d\mu}$ and $n_{v\mu}$ represent the density-of-state effective mass with $m_{d\mu} = \sqrt{m_{y\mu}m_{z\mu}}$ and the degeneracy of the μth group, respectively. From Eq. (5), one can show that the electric field at near $x = 0$ is given by the

following formula:

$$\mathcal{E} = \frac{e}{\epsilon_s}\int_0^{W_d}dx'\left[n(x') + N_a\right], \qquad (7)$$

where the width of the depletion region becomes maximum in the strong inversion regime such that $W_d \cong \left(2\epsilon_sE_g/e^2N_a\right)^{1/2}$ with E_g being the energy gap of the semiconductor. We solve the coupled equations of Eqs. (4) and (5), which is called the Schrödinger-Poisson equation. For practical applications, we choose the p-type Si(100) as an active layer with the following set of parameters: $\epsilon_s = 11.7, N_a = 1.0 \times 10^{15}$ cm$^{-3}, m_l = 0.98m_e, m_t = 0.19m_e, m_c^* = 0.26m_e$, and $W_d = 1.36$ μm. At room temperature, the electron mobility μ_e for high purity silicon can reach about 1400 cm^2/Vs at low doping and hence one can estimate that the plasma damping rate $\nu = e/(m_c^*\mu_e) \cong 4.2 \times 10^{12}$ Hz. For Si(100) substrate, the six symmetry-related ellipsoidal electron pockets are split into the following two groups: For $\mu = 1$, $(m_x, m_y, m_z) =$
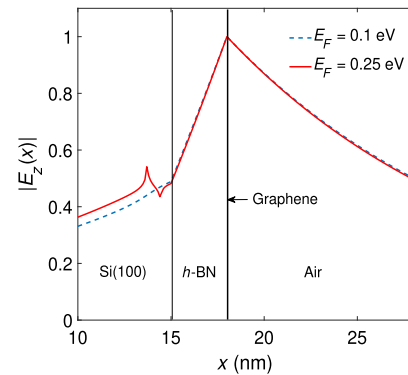

FIG. 7. $|E_z(x)|$ is plotted as a function of x for two values of $E_F = 0.1, 0.25$ eV. Here $|E_z(x)|$ is normalized by the value at graphene. For $E_F > E_F^*$, $|E_z(x)|$ exhibits a sharp deviation from the field profile for $E_F = 0.1$ eV due to the resonant coupling to the local plasmon resonance inside the p-type Si(100) layer.
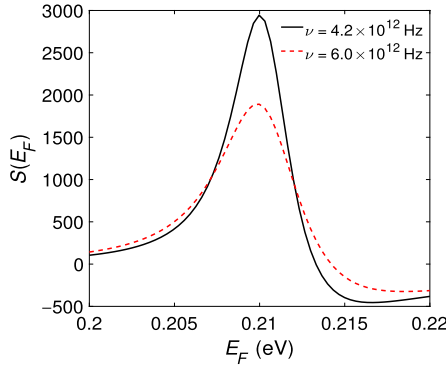
FIG. 8. $S(E_F)$ is plotted as a function of E_F for two values of plasma damping rate $\nu = 4.2 \times 10^{12}, 6 \times 10^{12}$ Hz. The sharpness of switching is measured by Q factor, which is given by $Q = E_{\text{FM}}/\Delta E_F$. Here $S(E_F)$ has a maximum value at E_{FM} and ΔE_F represents the FWHM. The black solid line describes $S(E_F)$ for $\nu = 4.2 \times 10^{12}$ Hz and $Q \cong 58$. The red dashed line describes $S(E_F)$ for $\nu = 6 \times 10^{12}$ Hz and $Q \cong 41$.

(m_l, m_t, m_t) with $n_v = 2$ and for $\mu = 2$, $(m_x, m_y, m_z) = (m_t, m_t, m_l)$ with $n_v = 4$ [41].

By numerically solving the Schrödinger-Poisson equation, we obtain $\mathcal{E} = 1$ MeV/cm for $E_F = 0.2$ eV and $\mathcal{E} = 1.6$ MeV/cm for $E_F = 0.3$ eV. In Fig. 3(a), the solid (dashed) curve describes the electron number density $n(x)$ as a function of $-x$ for $E_F = 0.2$ eV($E_F = 0.3$ eV). In Fig. 3(b), the real part of dielectric permittivity $\text{Re}[\epsilon(x)]$ is plotted as a function of $-x$ in the solid (dashed) curve for $E_F = 0.2$ eV($E_F = 0.3$ eV). One can notice that for $E_F = 0.3$ eV, $\text{Re}[\epsilon(x)]$ becomes negative for certain regions of x. At the critical value of E_F^*, a transition occurs locally from dielectric to metal, where the real part of local dielectric permittivity changes sign. When E_F increases above a critical value of E_F^*, $\text{Re}[\epsilon(x)]$ crosses to zero at two positions $x = x_1, x_2$ in the inversion layer, which induces a local plasmon resonance. This significantly increases the impedance of the active layer, since the dominant contribution to the impedance change comes from the term

$-ik_z^2/[k\epsilon(\omega, x)]$ in Eq. (2) and becomes singular at $x = x_1, x_2$ [11]. At the top of the active layer, the real part of the impedance change $\Delta Z = Z(0) - Z_0$ from the bulk value Z_0 is obtained as follows:

$$\text{Re}(\Delta Z) = \text{Re}\left[-\frac{ik_z^2}{k}\int_{-L}^{0} dx \frac{1}{\epsilon(\omega, x)}\right] \cong \frac{\pi k_z^2}{k\epsilon_\infty}\sum_{i=1,2}\left|\frac{d\ln n}{dx_i}\right|^{-1}, \tag{8}$$

where $Z_0 = (i/\epsilon_\infty)\sqrt{k_z^2/k^2 - \epsilon_\infty}$ and we assume that $\omega \gg \nu$ and $L > W_d$. We numerically calculate $\text{Re}(\Delta Z)$ as a function of the Fermi energy E_F for $\lambda = 8$ μm. Figure 4 demonstrates a dramatic increase of $\text{Re}(\Delta Z)$ above $E_F^* \cong 0.21$ eV.

Now we want to show that the transmission of the SPP is suppressed due to the coupling to the local plasmon resonance above E_F^*. The impedance $Z(x)$ is a continuous function of x except for the graphene layer. The boundary conditions for $H_y(x)$ and $E_z(x)$ at the graphene layer yield the following boundary condition for the impedance:

$$Z^{-1}(d^+) - Z^{-1}(d^-) = \frac{\sigma_\Sigma(\omega)}{\epsilon_0 c}, \tag{9}$$

where d is the thickness of the h-BN layer, $Z(d^+)$ represents the impedance right above the graphene layer, and $Z(d^-)$ the impedance right below the graphene layer. Here $Z(d^+)$ is described by the impedance of air, which is written by $Z(d^+) = -(i/\epsilon_0)\sqrt{k_z^2/k^2 - \epsilon_0}$. In the terahertz and midinfrared regime, the optical conductivity of graphene $\sigma_\Sigma(\omega)$ is well described by the following formula:

$$\sigma_\Sigma(\omega) = \frac{e^2\epsilon_F}{\pi\hbar^2}\frac{i}{\omega + i\tau^{-1}}, \tag{10}$$

where the Fermi energy of graphene is given by $\epsilon_F = \hbar v_F\sqrt{\pi n}$ with n and v_F being the electron number density and the Fermi velocity, respectively. For the exfoliated graphene, it is experimentally demonstrated that $v_F \cong 10^6$ m/s, $\mu_e \cong 10^4$ cm²/Vs, and $\tau = \mu_e\epsilon_F/(ev_F^2)$ [17].
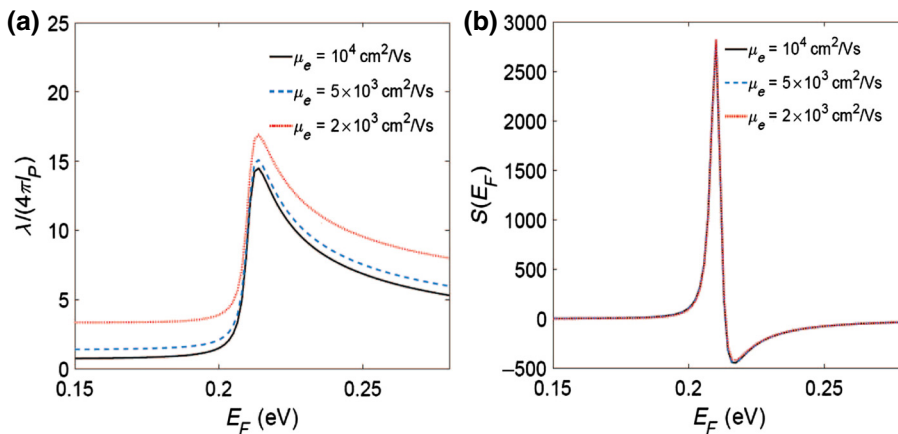

FIG. 9. (a) For the fixed value of $\epsilon_F = 0.4$ eV, $\lambda/(4\pi l_p)$ is plotted as a function of E_F for three different values of electron mobility of graphene $\mu_e = 10^4, 5 \times 10^3, 2 \times 10^3$ cm²/Vs. (b) The corresponding function $S(E_F)$ is plotted as a function of E_F for three different values of electron mobility of graphene.
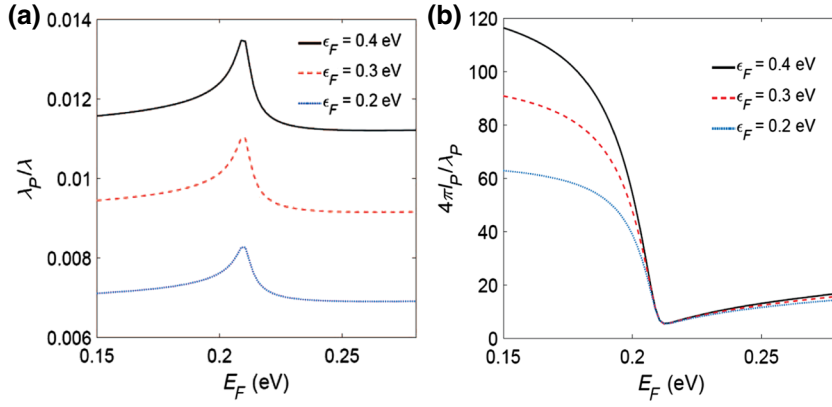
FIG. 10. (a) The wavelength of the SPP is plotted as a function of E_F in units of λ for $\epsilon_F = 0.2, 0.3, 0.4$ eV. One notices that λ_p increases with the increase of ϵ_F at the fixed E_F. (b) The ratio of the propagation length to the wavelength of the SPP is plotted as a function of E_F for $\epsilon_F = 0.2, 0.3, 0.4$ eV. One clearly sees that $4\pi l_p/\lambda_p$ increases with the Fermi energy of graphene below E_F^*.

When the h-BN layer is thick enough to neglect the coupling to the active layer, one can approximate that $Z(d^-) \cong (i/\epsilon_{BN})\sqrt{k_z^2/k^2 - \epsilon_{BN}}$. In this limit, the dispersion relation of the SPP is obtained by solving the following equation:

$$\frac{\epsilon_0}{\sqrt{k_z^2 - \epsilon_0 k^2}} + \frac{\epsilon_{BN}}{\sqrt{k_z^2 - \epsilon_{BN} k^2}} = \frac{4\alpha\epsilon_F}{\hbar k}\frac{1}{\omega + i\tau^{-1}}, \quad (11)$$

which agrees exactly with the equation obtained by Jablan *et al.* [25]. For the fixed frequency ω of an incident light, one can obtain the complex-valued wave number k_z by solving Eq. (11). The SPPs thus obtained are a type of surface wave, guided along the interface in much the same way as light is guided by an optical fiber. Their wavelengths are much shorter than that of an incident light. Hence, they can have tighter spatial confinement and higher local field intensity. Perpendicular to the interface, they have subwavelength-scale confinement. The SPP propagates along the interface until its energy is lost either by absorption in the metal or scattering into other directions. The wavelength of the SPP is given by $\lambda_p = 2\pi/\mathrm{Re}\,(k_z)$. The propagation length of the SPP is defined as the distance for the SPP intensity to decay by a factor of $1/e$, which is written as $l_p = 1/[2\mathrm{Im}\,(k_z)]$. Since $|k_z/k| \gg 1$, the dispersion relation and the propagation length of the SPP is given by $\omega = \{e^2\epsilon_F/[(\epsilon_0 + \epsilon_{BN})\pi\hbar^2]\}^{1/2}\sqrt{\mathrm{Re}\,(k_z)}$ and $l_p = (\omega\tau/4\pi)\,\lambda_p$, respectively.

III. NUMERICAL RESULTS AND DISCUSSION

For relatively thin film of the h-BN layer with thickness $d \ll \lambda_p$, the SPP is strongly coupled to the active layer. For an incident light with midinfrared wavelength $\lambda = 8$ μm and the exfoliated graphene with $\epsilon_F = 0.4$ eV, we calculate the complex-valued wave number k_z as a function of the Fermi energy E_F by numerically solving Eq. (2). The thickness of the h-BN layer has been taken to be 3 nm, which is thick enough to function as a gate dielectric [42,43], and that of the p-type Si layer $L > W_d$. Recent experiments have demonstrated that for the h-BN film with thicknesses below 10 nm, the dielectric breakdown voltage increases linearly with the film thickness

and the breakdown electric field remains above 4 MV/cm [43]. In Fig. 5, the electric field strength $\mathcal{E}$ at the gate dielectric-semiconductor interface is plotted as a function of the Fermi energy E_F for $\lambda = 8$ μm. At the critical value of $E_F^* \cong 0.21$ eV, $\mathcal{E} \cong 1.0$ MV/cm. In Fig. 6(a), the wavelength of the SPP is plotted as a function of E_F. The wavelength λ_p of the SPP shows a nonmonotonic dependence on E_F, as it passes through the critical value. But it remains to be on the order of approximately $1/100$ of that of an incident light. This makes graphene a promising material for practical application to subwavelength plasmonic devices. In Fig. 6(b), the ratio of the propagation length to the wavelength of the SPP is plotted as a function of E_F. One clearly notices that $4\pi l_p/\lambda_p$ is significantly reduced by a factor of approximately 21 upon switching at $E_F^* \cong 0.21$ eV compared to the value at $E_F = 0.15$ eV. We also confirm that the propagation length of the SPP is reduced by a factor of approximately 19 upon switching. In Fig. 7, the electric field profile $|E_z(x)|$ is plotted as a function of x for two values of $E_F = 0.1, 0.25$ eV. Here $|E_z(x)|$ is normalized by the value at graphene. For $E_F > E_F^*$, $|E_z(x)|$ exhibits a sharp deviation from the field profile for $E_F = 0.1$ eV due to the resonant coupling to the
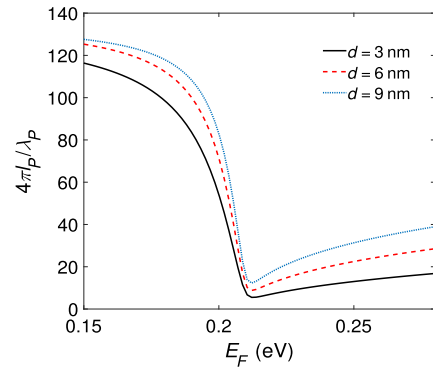

FIG. 11. The ratio of the propagation length to the wavelength of the SPP is plotted as a function of E_F for three different values of h-BN thicknesses $d = 3, 6, 9$ nm at a fixed value of $\epsilon_F = 0.4$ eV.
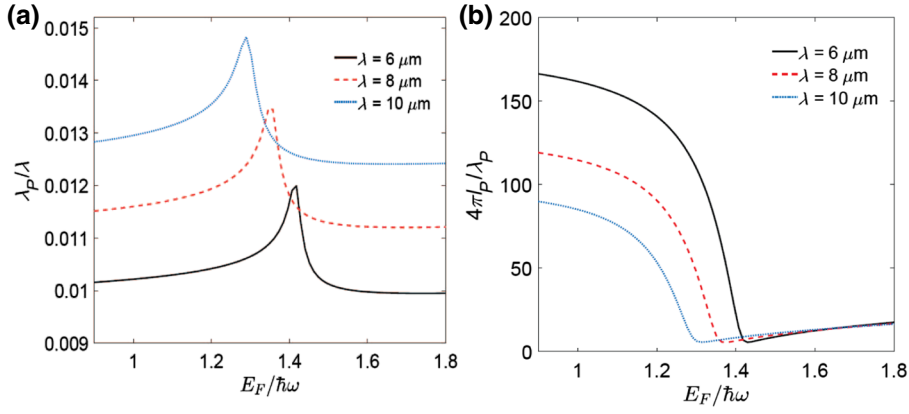
FIG. 12. (a) The wavelength of the SPP is plotted as a function of $E_F/\hbar\omega$ in units of λ for $\lambda = 6, 8, 10 \mu m$. (b) The ratio of the propagation length to the wavelength of the SPP is plotted as a function of $E_F/\hbar\omega$ for $\lambda = 6, 8, 10$ μm.

local plasmon resonance inside the p-type Si(100) layer. This demonstrates that our device can effectively operate as a subwavelength plasmonic switch for the SPP.

As E_F goes beyond the critical value E_F^*, the propagation length l_p of the SPP exhibits a dramatic decrease. In order to estimate the sharpness of switching, we define the function $S(E_F)$ as follows: $S(E_F) = \partial \left[\lambda/(4\pi l_p) \right]/\partial E_F$. In Fig. 8, $S(E_F)$ is plotted as a function of E_F for two different values of plasma damping rate $\nu = 4.2 \times 10^{12}, 6 \times 10^{12}$ Hz. The sharpness of switching is measured by Q factor, which is defined by $Q = E_{\text{FM}}/\Delta E_F$. Here $S(E_F)$ has a maximum value at E_{FM} and ΔE_F represents the FWHM. The black solid line describes $S(E_F)$ for $\nu = 4.2 \times 10^{12}$ Hz. One estimates that $Q \cong 58$. The red dashed line describes $S(E_F)$ for $\nu = 6 \times 10^{12}$ Hz. One estimates that $Q \cong 41$. In Fig. 9(a), $\lambda/(4\pi l_p)$ is plotted as a function of E_F for three different values of electron mobility of graphene $\mu_e = 10^4, 5 \times 10^3, 2 \times 10^3 \text{cm}^2/\text{Vs}$ for the fixed value of $\epsilon_F = 0.4$ eV. One can notice that as μ_e decreases, there exists an overall increase in $\lambda/(4\pi l_p)$. In Fig. 9(b), the corresponding function $S(E_F)$ is plotted as a function of E_F for three different values of μ_e. It clearly demonstrates that the sharpness of switching line shape has a negligible dependence on the electron mobility of graphene for the fixed value of ϵ_F. Hence we confirm that the sharpness of switching line shape mainly depends on the plasma damping rate ν of the active layer. In Fig. 10(a), λ_p/λ is plotted as a function of E_F for $\epsilon_F = 0.2, 0.3, 0.4$ eV. One notices that λ_p increases with the increase of ϵ_F at the fixed E_F. For $E_F < E_F^*$, this is easily understood from the following formula: $\omega \cong \{e^2 \epsilon_F/[(\epsilon_0 + \epsilon_{\text{BN}})\pi \hbar^2]\}^{1/2} \sqrt{\text{Re}(k_z)} \propto (\epsilon_F/\lambda_p)^{1/2}$. Hence λ_p increases linearly with ϵ_F for the fixed frequency ω as shown in Fig. 10(a). In Fig. 10(b), $4\pi l_p/\lambda_p$ is plotted as a function of E_F for $\epsilon_F = 0.2, 0.3, 0.4$ eV. One clearly sees that $4\pi l_p/\lambda_p$ increases with the Fermi energy of graphene below E_F^*. Below E_F^*, this is easily understood through the following relation: $4\pi l_p/\lambda_p \cong \omega\tau \propto \epsilon_F$, since $\tau = \mu_e \epsilon_F/(ev_F^2)$. Hence $4\pi l_p/\lambda_p$ increases linearly with ϵ_F. In Fig. 11, $4\pi l_p/\lambda_p$ is plotted as a function of

E_F for different values of h-BN thicknesses $d = 3, 6, 9$ nm. There exists only a modest change in the switching line shape for varying thicknesses. In Fig. 12(a), λ_p/λ is plotted as a function of $E_F/\hbar\omega$ for $\lambda = 6, 8, 10$ μm. One notices that while the critical value of Fermi energy increases with the decrease of λ, λ_p/λ decreases with the decrease of λ. In Fig. 12(b), $4\pi l_p/\lambda_p$ is plotted as a function of E_F for $\lambda = 6, 8, 10$ μm. One clearly notices that $4\pi l_p/\lambda_p$ increases with the decrease of λ below E_F^*.

IV. CONCLUSION

To summarize, we propose a subwavelength plasmonic waveguide based on graphene, which can effectively gate the transmission of the SPP by varying gate voltage. As a van der Waals material, thin h-BN film is chosen to be a gate dielectric material to support the high mobility of graphene. For practical applications, we choose the p-type Si(100) as an active layer. Graphene plasmonics have practical application ranges from terahertz to midinfrared regime. For an incident light with midinfrared wavelength $\lambda = 8$ μm, we demonstrate that the wavelength of the SPP is reduced below $1/100$ of that of an incident light. By applying the gate voltage, the propagation length of the SPP is reduced by a factor of approximately 20 upon switching, which exhibits the sharp switching line shape. Our theoretical results strongly support that our plasmonic waveguide can effectively operate as a subwavelength plasmonic switch for the SPP.

[1] A. Krasavin, K. MacDonald, N. Zheludev, and A. Zayats, High-contrast modulation of light with light by control of surface plasmon polariton wave coupling, Appl. Phys. Lett. **85**, 3369 (2004).

[2] T. Nikolajsen, K. Leosson, and S. Bozhevolnyi, Surface plasmon polariton based modulators and switches operating at telecom wavelengths, Appl. Phys. Lett. **85**, 5833 (2004).

[3] R. Pala, K. Shimizu, N. Melosh, and M. Brongersma, A nonvolatile plasmonic switch employing photochromic molecules, Nano Lett. **8**, 1506 (2008).

[4] M. Dicken, L. Sweatlock, D. Pacifici, H. Lezec, K. Bhattacharya, and H. Atwater, Electrooptic modulation in thin film barium titanate plasmonic interferometers, Nano Lett. **8**, 4048 (2008).

[5] J. Dionne, K. Diest, L. Sweatlock, and H. Atwater, PlasMOStor: A metal-oxide-Si field effect plasmonic modulator, Nano Lett. **9**, 897 (2009).

[6] M. Abb, P. Albella, J. Aizpurua, and O. Muskens, All-optical control of a single plasmonic nanoantenna-ITO hybrid, Nano Lett. **11**, 2457 (2011).

[7] S. Zeng, D. Baillargeat, H. Ho, and K. Yong, Nanomaterials enhanced surface plasmon resonance for biological and chemical sensing applications, Chem. Soc. Rev. **43**, 3426 (2014).

[8] W. Barnes, A. Dereux, and T. Ebbesen, Surface plasmon subwavelength optics, Nature **424**, 824 (2003).

[9] P. Huidobro, M. Nesterov, L. Martin-Moreno, and F. Garcia-Vidal, Transformation optics for plasmonics, Nano Lett. **10**, 1985 (2010).

[10] E. Ozbay, Plasmonics: Merging photonics and electronics at nanoscale dimensions, Science **311**, 189 (2006).

[11] Y. Akimov and H. Chu, Plasmon-plasmon interaction: Controlling light at nanoscale, Nanotechnology **23**, 444004 (2012).

[12] J. Chen, G. Smolyakov, S. Brueck, and K. Malloy, Surface plasmon modes of finite, planar, metal-insulator-metal plasmonic waveguides, Opt. Express **16**, 14902 (2008).

[13] J. Jacob, A. Babua, G. Mathew, and V. Mathew, Propagation of surface plasmon polaritons in anisotropic MIM and IMI structures, Superlattice. Microst. **44**, 282 (2008).

[14] T. Davis, Surface plasmon modes in multi-layer thin-films, Opt. Commun. **282**, 135 (2009).

[15] X. Zhu, J. Zhang, J. Xu, H. Li, X. Wu, Z. Liao, Q. Zhao, and D. Yu, Dispersion control in plasmonic open nanocavities, ACS Nano **5**, 6546 (2011).

[16] M. Kim, S. Lee, M. Choi, B. Ahn, N. Park, Y. Lee, and B. Min, Low-loss surface-plasmonic nanobeam cavities, Opt. Express **18**, 11089 (2010).

[17] A. Geim and K. Novoselov, The rise of graphene, Nat. Mater. **6**, 183 (2007).

[18] K. Novoselov, V. Fal'ko, L. Colombo, P. Gellert, M. Schwab, and K. Kim, A roadmap for graphene, Nature **490**, 192 (2012).

[19] A. K. Geim, Graphene: Status and prospects, Science **19**, 1530 (2009).

[20] C. Lee, X. Wei, J. Kysar, and J. Hone, Measurement of the elastic properties and intrinsic strength of monolayer graphene, Science **18**, 385 (2008).

[21] A. Balandin, Thermal properties of graphene and nanostructured carbon materials, Nat. Mater. **10**, 569 (2011).

[22] T. Constant, S. Hornett, D. Chang, and E. Hendry, All-optical generation of surface plasmons in graphene, Nat. Phys. **12**, 124 (2016).

[23] L. Wong, I. Kaminer, O. Ilic, J. Joannopoulos, and M. Soljačić, Towards graphene plasmon-based free-electron infrared to X-ray sources, Nat. Photonics **10**, 46 (2016).

[24] T. Low and P. Avouris, Graphene plasmonics for terahertz to mid-infrared applications, ACS Nano **8**, 1086 (2014).

[25] M. Jablan, H. Buljan, and M. Soljacic, Plasmonics in graphene at infrared frequencies, Phys. Rev. B **80**, 245435 (2009).

[26] Z. Fei, A. Rodin, G. Andreev, W. Bao, A. McLeod, M. Wagner, L. Zhang, Z. Zhao, M. Thiemens, G. Dominguez, M. Fogler, A. Castro Neto, C. Lau, F. Keilmann, and D. Basov, Gate-tuning of graphene plasmons revealed by infrared nano-imaging, Nature **487**, 82 (2012).

[27] J. S. Gómez-Díaz and J. Perruisseau-Carrier, Graphene-based plasmonic switches at near infrared frequencies, Opt. Express **21**, 15490 (2013).

[28] A. N. Grigorenko, M. Polini, and K. S. Novoselov, Graphene plasmonics, Nat. Photonics **6**, 749 (2012).

[29] F. H. Koppens, D. E. Chang, and F. J. G. de Abajo, Graphene plasmonics: A platform for strong light-matter interactions, Nano Lett. **11**, 3370 (2011).

[30] A. Ferreira, N. M. R. Peres, and A. H. Castro Neto, Confined magneto-optical waves in graphene, Phys. Rev. B **85**, 205426 (2012).

[31] J. S. Gómez-Díaz and J. Perruisseau-Carrier, Charge carrier relaxation and effective masses in silicon probed by terahertz spectroscopy, J. Appl. Phys. **112**, 124906 (2012).

[32] Yu Zhou, Cheng Wang, DiHu Xu, RenHao Fan, Kun Zhang, RuWen Peng, Qing Hu, and Mu Wang, Tuning the dispersion relation of a plasmonic waveguide via graphene contact, Europhys. Lett. **107**, 34007 (2014).

[33] Yu Zhou, YingYing Zhu, Kun Zhang, HongWei Wu, RuWen Peng, RenHao Fan, and Mu Wang, Plasmonic band structures in doped graphene tubes, Opt. Express **25**, 12081 (2017).

[34] T. Echtermeyer, L. Britnell, P. Jasnos, A. Lombardo, R. Gorbachev, A. Grigorenko, A. Geim, A. Ferrari, and K. Novoselov, Strong plasmonic enhancement of photovoltage in graphene, Nat. Commun. **2**, 458 (2011).

[35] M. Jadidi, A. Sushkov, R. Myers-Ward, A. Boyd, K. Daniels, D. Kurt Gaskill, M. Fuhrer, H. Drew, and T. Murphy, Tunable terahertz hybrid metal-graphene plasmons, Nano Lett. **15**, 7099 (2015).

[36] A. Fernandez-Dominguez, F. Garcia-Vidal, and L. Martin-Moreno, Unrelenting plasmons, Nat. Photonics **11**, 8 (2017).

[37] C. Dean, A. Young, I. Meric, C. Lee, L. Wang, S. Sorgenfrei, K. Watanabe, T. Taniguchi, P. Kim, K. Shepard, and J. Hone, Boron nitride substrates for high-quality graphene electronics, Nat. Nanotechnol. **5**, 722 (2010).

[38] R. V. Gorbachev, A. S. Mayorov, A. K. Savchenko, D. W. Horsell, and F. Guinea, Conductance of p-n-p graphene structures with 'air-bridge' top gates, Nano Lett. **8**, 1995 (2008).

[39] V. L. Ginzburg, *The Propagation of Electromagnetic Waves in Plasmas* (Pergamon Press, Oxford, New York, 1970).

[40] C. W. Lee and J. G. Hwu, Quantum-mechanical calculation of carrier distribution in MOS accumulation and strong inversion layers, AIP Adv. **3**, 102123 (2013).

[41] F. Stern and W. E. Howard, Properties of semiconductor surface inversion layers in the electric quantum limit, Phys. Rev. **163**, 816 (1967).

[42] P. Sutter, J. Lahiri, P. Zahl, B. Wang, and E. Sutter, Scalable synthesis of uniform few-layer hexagonal boron nitride dielectric films, Nano Lett. **13**, 276 (2013).

[43] S. K. Jang, J. Youn, Y. J. Song, and S. Lee, Synthesis and characterization of hexagonal boron nitride as a gate dielectric, Sci. Rep. **6**, 30449 (2016).